Design and characterization of a near-field gamma imager for in situ measurements of fuel rod deformations

Guillaume Amoyal, Vincent Schoepff, Frédérick Carrel, Maxime Morenas, Dorin Dusciac

Design and characterization of a near-field gamma imager for *in situ* measurements of fuel rod deformations

G. Amoyal[(a)], V. Schoepff[(a)], F. Carrel[(a)], M. Morenas[(a)], D. Dusciac[(b)]
[(a)] *Université Paris-Saclay, CEA, List, F-91120 Palaiseau, France.*
[(b)] *Université Paris-Saclay, CEA, List, Laboratoire National Henri Becquerel (LNE-LNHB), F-91120 Palaiseau, France.*

ABSTRACT

A prototype of gamma imaging system has been developed for the detection of fuel rod deformations, based on the WidePIX hybrid pixel detector, associated with a collimator. The WidePIX detector used in the frame of these developements is made of 2×5 Timepix devices hybridized with a 1 mm-thick cadmium telluride semiconductor. A specific collimator was designed, offering the best compromise between mechanical feasibility, cost, signal-to-noise ratio and angular resolution, and making it possible to visualize the fuel rod deformations. In this work, we present the design of the collimator carried out by Monte-Carlo simulation, and experimental results obtained with this prototype on a Cs-137 and Co-60 metrological irradiator.

I. INTRODUCTION

The study of accidental situations is one of the major concern for nuclear industry in guaranteeing the so-called regulated safety of its electricity production facilities. The Loss Of Coolant Accident (LOCA) is tested in experimental reactor and hot cell to verify the mechanical properties of the fuel rod, the safety criteria and the associated calculation codes. The VINON-LOCA experimental set-up in CEA Cadarache, aims at observing, online, the Fuel Fragmentation, Relocation and Dispersal (FFRD) during a LOCA sequence [1]. The tests consist in placing a fuel rod in a shielded cell, which will be heated by magnetic induction in order to reproduce the temperature conditions of the first phase of a LOCA transient. Instrumentation positioned in the cell will be located close to the fuel rod in order to monitor its behaviour during heating. Currently, monitoring of fuel relocation is carried out by means of a collimated gamma spectrometer, which only allows the visualization of a small part of the fuel rod. This technique has several limitations, it is not adapted to fast kinetics, and does not allow the integrity of the fuel rod to be visualized. Thus, if the relocation of the fuel occurs in a part of the fuel rod that is not in the gamma spectrometer's sight, then this part will only be visualized *a posteriori*. In the frame of this study, the gamma imaging measurement technique is used to quantify the fuel rod deformation, enabling real-time monitoring of the phenomenon with a larger field of view. In this context, we have designed and developed, in partnership with CEA Cadarache, EDF [2], and Framatome [3], a gamma imager to monitor the deformation of the fuel rod. The gamma-rays, which will enable the swelling to be monitored, are derived from the fission products of the pre-irradiated rod. Due to the constraints imposed by the hot cell measurement, the developed gamma imaging system should be located at a distance of 25 cm from the fuel rod. At this distance, the dose rate at the gamma imaging system will be of the order of 500 $mGy.h^{-1}$. This constraint regarding the high dose rate must absolutely be taken into account in the designing process of the system. Preliminary experimental tests carried out at the LAMIR Laboratory of CEA Cadarache have estimated that the variation in the radius of the fuel rod during heating is 2 to 3 mm, over a total length of roughly 16 mm.

Hence, the developments presented in this article are positioned in the context of near-field gamma imaging in highly irradiating conditions. The work presented therefore concerns, firstly, the design of a collimator offering the best compromise between mechanical feasibility, cost, signal-to-noise ratio and angular resolution, thus making it possible to visualize the deformations of the fuel rod, and secondly, an evaluation of the experimental performance of the proposed gamma imager in metrological laboratory conditions.

The detector used is the WidePIX pixelated detector [4], the latter was chosen in particular because it has a pixelated detection area of 2.8×7.04 cm^2, i.e., approximately 20 cm^2, allowing the part of the fuel rod subjected to heating to be visualized with a single detector. In addition to positions of interactions, the detector also provides their energies.

The collimator was dimensioned using Monte-Carlo simulations. Among the main assumptions, we chose to design the collimator with the most energetic gamma-rays emitted by the radioisotope with the highest photon flux, namely Cs-137 emitting gamma-rays of 661.7 keV.

Preliminary experimental measurements were then carried out on a multi-sources irradiator located at the Henri Becquerel National Laboratory (LNHB) of CEA Paris-Saclay, France. A second measurement campaign was carried out at the CEA Cadarache LAMIR facilities to verify the magnetic compatibility between the gamma imager, and the magnetic coil that will heat the fuel rod during the final test.

II. Material and Methods

A. The WidePIX detector

WidePIX is a pixelated detector, developed by ADVACAM s.r.o., based on Timepix technology, a CMOS pixel detector readout chip developed by CERN [5]. WidePIX can either be composed of 1×5 or 2×5 Timepix devices hybridized with a 300 µm-thick silicon semiconductor or 1 mm-thick cadmium telluride (CdTe) semiconductor, which respectively corresponds to a sensitive area of 14×70.4 mm² or 28×70.4 mm². The sensitive area is composed of squared pixel with a pitch of 55 µm. In the context of our developments, the widest sensitive area is required, and the material must have the largest possible effective atomic number. Therefore, the WidePIX detector used in the framework of this project is composed of a sensitive area of 28×70.4 mm², equivalent to 512×1280, or 655360, squared pixels, hybridized with a 1 mm-thick CdTe semiconductor.
The WidePIX detector is used in "Timepix" mode, providing information of interactions positions and the associated energy deposited. The energy deposited is measured using the Time-Over-Threshold (ToT) method [6]. The detector readout is frame based, for a number of N frames with a duration specified by the user; the data is stored as N matrices of 512×1280 ToT values (1.3 Mo per frame). The intrinsic dead time of the detector between each frame is 0.2 sec.
The detector is controlled using the PixetPro software version 1.7.5.915, developed by ADVACAM s.r.o. A USB communication is used between the WidePIX detector and the acquisition computer.

B. The collimator

The collimator is a key part of a gamma imaging system. It is an element composed of transparent and opaque elements with a given pattern. Classical gamma cameras mainly use a coded-aperture to spatially modulate the incoming gamma-rays and localize radioactive hotspots [7]. However, the environment of the VINON-LOCA experiment requires the future gamma imager to be positioned at a distance of about 25 cm from the fuel rod to be imaged. The design of the collimator was therefore inspired by developments in near field imaging in the medical field.
In near-field imaging, the objective of a collimator is to let through only the gamma-rays arriving perpendicularly to the detector. Each pinhole therefore images a given region with a very restricted field of view. The field of view of the collimator is larger the more pinholes there are. In medical imaging, several collimator designs exist [11][12]: collimator with parallel-holes, the pinhole, the diverging collimator and the converging collimator. The parallel-hole collimator has three main advantages with respect to the application targeted by these developments: it has a wide field of view, and its sensitivity does not decrease with the distance from the object [11]. Furthermore, the manufacturing process of a parallel-hole collimator is the simplest of the other configurations presented above. For these reasons, the choice of collimator was made in favour of a parallel-hole collimator, the dimensioning of which is presented in section III.

C. Monte-Carlo simulations setup

In the frame of this study, Monte-Carlo (MC) simulations are used to design the collimator of the gamma ray imaging system. The numerical simulations are carried using MCNP6.1 [13]. The simulated system consists of three different elements: the source term describing the fuel rod to be imaged; the imager composed of a sensitive volume in which photons will interact; and a collimator, which is the key part of this MC dimensioning.

1) Source term

The object to be imaged in this project is an irradiated fuel rod with localised radial deformation. Table I summarizes the main gamma emitters of a 47.5 GWj.t^{-1} irradiated fuel rod after 4 years of cooling. It was chosen to design the collimator with a gamma ray flux greater than 10^{15} s^{-1}.tUie^{-1}, identified in bold in Table I. During a LOCA phase, the highly volatile cesium will tend to accumulate between the fuel fragments, while the barium forms oxide precipitates in the uranium oxide matrix [14]. It is subsequently assumed that the gamma emitters are uniformly distributed in the fuel rod.

Table I: Main gamma-rays emitting radionuclides of a fuel rod irradiated at 45.7 GWj.t^{-1} after 4 years of cooling [14] *(translated from French), their associated energies* [15]*, and the associated gamma ray flux.*

Radionuclide	Estimated activity (Bq.tU$_{ie}^{-1}$)	Energy of gamma-rays (keV)	Gamma ray flux (s^{-1}. tU$_{ie}^{-1}$)
Cs-137	5.0×10^{15}	**661.7**	**8.57×10^{15}**
Cs-134	2.5×10^{15}	**604.7**	**2.45×10^{15}**
		795.9	**2.13×10^{15}**
		569.3	3.75×10^{14}
		802.0	2.00×10^{14}
		563.2	2.00×10^{14}
Rh-106	1.6×10^{15}	511.9	3.68×10^{14}
		621.9	1.60×10^{14}

tU$_{ie}$: Tonne of initial enriched Uranium.

The simulated fuel rod geometry was defined using preliminary results obtained by the LAMIR laboratory of CEA Cadarache: a radial deformation length of the fuel rod about 16 mm, and an increase in the radius of the fuel rod about 2 mm. Thus, the volume of the simulated source is defined as a cylindrical volume with an initial diameter of 8 mm that corresponds to the characteristic dimension of unirradiated fuel rod cladding, and at mid-height, the fuel rod is deformed by increasing its radius by 2 mm over a length of 4 mm. It was deliberately chosen to reduce the length of the deformation zone in the simulation files, in order to reduce the simulation time. The composition of the fuel rod is estimated as follows: one volume of uranium oxide with a density of 10.97 g.cm^{-3}; contained in a zirconium alloy cladding with a thickness of 0.57 mm, an external diameter of 9.5 mm, and a density of 6.52 g.cm^{-3}. In addition, assuming that the fuel relocates following swelling, the choice was made to simulate fuel rods with constant volume activity. During the rod deformation, its activity increases proportionally to its volume increase, as described by equation (II-1. In equation (II-1, N_{t0} and N_{ti} are respectively the number of simulated particles for an intact fuel rod and for a deformation i of the latter; V_0 and V_i are respectively the volume of the intact fuel rod, and with a deformation i.

$$N_{ti} = \frac{V_i}{V_0} * N_{t0} \qquad \text{(II-1)}$$

2) The sensitive volume and the collimator

The sensitive volume corresponds to the semiconductor of the WidePIX detector. It is simulated by a volume of CdTe with a density of 5.6 g.cm^{-3}. In order to reduce the simulation time, it was chosen to simulate a detection volume whose dimensions are 14×14 mm², composed of 256×256 squared pixels with a pixel pitch of 55 µm and a thickness of 1 mm. The different pixels are simulated using a lattice, in which an F8 Tally, that describes the energy distribution of pulses created in a detector, is used. Similarly, the simulated collimator covers the detection volume and has an area of 14×14 mm². Figure 1 shows an illustration of the simulated system, composed of the fuel rod emitting gamma-rays of 661.7 keV, at a distance of 25 cm of the collimator, which is placed between the CdTe volume and the fuel rod.

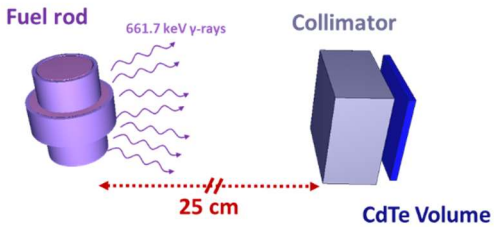

a

Figure 1: Illustration of the simulated system, with the three main blocks: the fuel rod emitting gamma-rays of 661.7 keV, the collimator, and athe CdTe volume.

D. The multi-sources irradiator of the LNHB

The multi-sources irradiator is located at the LNHB of CEA List on the Paris-Saclay site, and is among the primary national references in the field of ionising radiation. This installation, which is also part of the Laboratoire National de Métrologie et d'Essais (LNE) [16], works under COFRAC accreditation [17]. This accreditation sets out, among other things, the fields of validity in terms of dose rate of primary references. In the framework of this project, experimental measurement were carried out on the Co-60 and Cs-137 irradiators [18].

III. Design of the Collimator

A. Geometrical properties of parallel-holes collimator

A parallel-hole collimator consists in a stack of pinholes containing a honeycomb structure [11], separated by a wall called septa. Among the characteristic quantities to be dimensioned regarding of the collimator are the geometry of the holes: their shape, their length, their diameter; and the septal thickness. The main characteristics of a parallel-hole collimator are illustrated in figure 2.

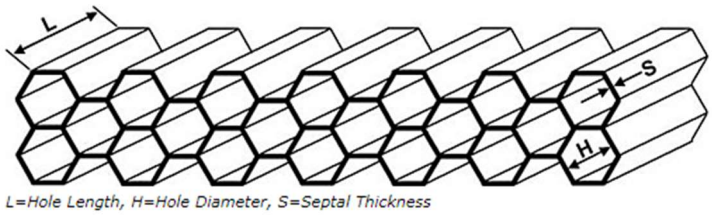

Figure 2: Scheme of the main characteristics of a parallel-hole collimator [19].

As described in [11], most of parallel-hole collimators have a honeycomb pattern with hexagonal holes, allowing the best fill factor. However, manufacturing hexagonal holes is complicated and expensive, especially when considering an intense incoming gamma-ray flux with energies greater than 600 keV. Therefore in order to ease the manufacturing process, it has been chosen to design a parallel-hole collimator with circular holes.

Assuming that septal penetration is zero, the spatial resolution of a parallel-hole collimator can be estimated by the equation (III-1) [20], in which δ is the spatial resolution, H is the diameter of holes, L is the thickness of the collimator, and z the distance between the object and the collimator. In the framework of these developments, the best spatial resolution is our key figure of merit. The lowest resolution is achieved when the object to be imaged is as close as possible to the collimator, which itself should be as thick as possible and have the smallest hole diameters. Reducing the diameter of the holes, however, directly causes a decrease in the sensitivity of the collimator. Nonetheless, this degradation in sensitivity is not relevant in view of the activity of the irradiated fuel rod.

$$\delta \approx H * \frac{L+z}{L} \qquad \textit{(III-1)}$$

Nervertheless, septal penetration is in practice not negligible given the energies of the gamma-rays involved. For a given diameter, the sizing of the septa results from a compromise between collimation and spatial resolution of the deformation. A thick septa improves the collimation of the divergent gamma beam by attenuation, while a thin septa maximises the useful detection area. The size of a septa therefore directly conditions the smallest deformation of the fuel rod that can be seen. It is the study of septal penetration for different collimator sizes that will be the subject of the MC simulations, the method and results of which are presented in section III.C.

B. Material of the collimator

The role of the collimator is to stop as many incident photons as possible that do not pass directly through its holes. The material (and also the thickness) of the collimator directly influence the sensitivity of the imager. These parameters determine the septal transparency, which is the proportion of photons of a given energy that pass through the septa. Table II shows the linear attenuation coefficient at 661.7 keV of different materials used to manufacture collimators. Gold and platinum are efficient but very expensive. Depleted uranium is a radioactive material that has the disadvantage of producing permanent background noise, and is also chemically toxic and restricted. Lead offers limited rigidity which can lead to a lack of precision when manufacturing or handling in the hot cell of the imager. Tungsten and tantalum offer excellent photon absorption at a reasonable raw material price. Since tungsten has a better linear stopping power than tantalum, the latter was chosen. However, as its machining is complicated, it was eventually decided to use a tungsten-based alloy called denal, composed roughly of 90-97 % of tungsten.

Table II: Linear attenuation coefficients for photons at 661.7 keV, and 20 °C, of different materials used to manufacture collimators. Coefficients are calculated from cross-sections of XCOM-NIST database [21].

Element	Lead	Tantalum	Tungsten	Gold	Platinum	Depleted Uranium
Symbol	Pb	Ta	W	Au	Pt	U-238
Linear attenuation coefficient for photons at 661.7 keV and 20 °C (cm^{-1})	1.17	1.49	1.78	1.92	2.09	2.32

C. Monte-Carlo simulations

1) Evaluated parameters

As described in sections A and 0, the choice of the collimator is a parallel circular hole collimator, with a honeycomb pattern, and made of denal. With these considerations in mind, the parameters to be determined are the thickness of the collimator, the diameter of the holes, and the septal thickness.

It was arbitrarily chosen to study collimator thicknesses between 5 and 9.5 cm. This choice is based on the laboratory's experience in ionising radiation imaging and on the potential presence of fission products in the fuel rod emitting gamma-rays with energy greater than 1 MeV.
The intrinsic spatial resolution of a collimator depends directly on the dimensions of the holes and septa. Because of the magnitude of the problem to be observed, the dimensions of the latter must be on a millimetre scale at most. On the other hand, manufacturing constraints limit the possible configurations. It was chosen to study diameters of holes with dimensions of 0.75 mm and 1 mm, and sizes of septa of 0.5 mm and 1 mm. Studied configurations are presented in Table III.

Table III: Configurations of the studied collimators by MC simulations.

Diameters of holes (mm)	Sizes of septa (mm)	Thicknesses (cm)
0.75	0.5	From 5 to 9.5
0.75	1	
1	0.5	
1	1	

2) Classification criterion

In order to evaluate the performances of the imaging system studied designs, a classification critera has been defined below. The objective is to count the energy deposits by characteristic area on the simulated images in order to determine a quantity equivalent to a signal to noise ratio (SNR). Three zones are distinguished for each simulated image, a so-called "direct" counting zone, equivalent to the signal, for which the incoming photons pass directly into the holes of the collimator; and two so-called "noisy" zones, for which the incident photons scatter in the collimator before interacting in the detection matrix. The different zones of "direct" and "noise" counts are shown in red and green respectively in figure 3.

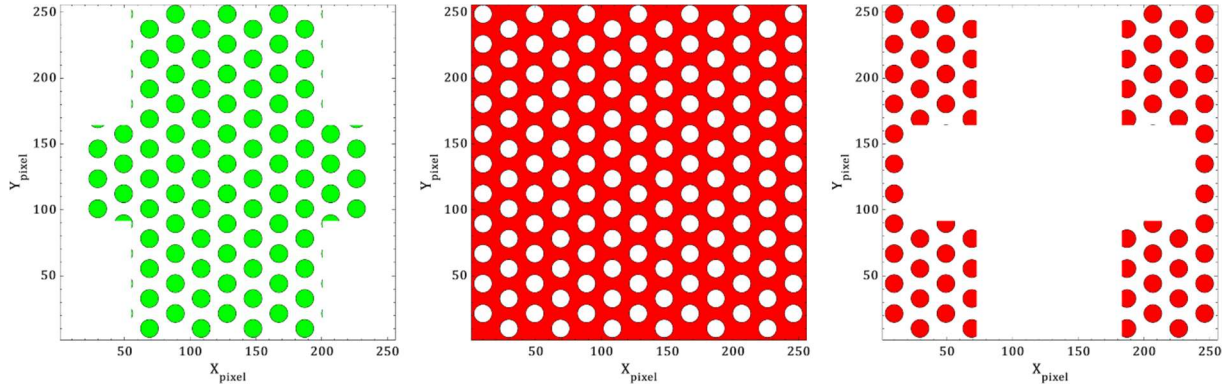

Figure 3:On the left, the "direct" count area, in green, corresponds to the signal; on the center and on the right, the "indirect" count area, equivalent to the noise, in red, respectively corresponding to photons interacting in the collimator, and photons penetrating the collimator.

Three count values are thus obtained, S_t (for straight photons) contributing to the “direct” count area; S_c (for scattered photons) and P_e (for penetrating photons) contributing to the “indirect” count area. The collimator configurations studied do not offer the same aperture area. In order to compare the different count values for each configuration, it was decided to normalise them by the ratio of the aperture area to the total area of the detector. SNR is then calculated using equation (III-2), in which, S_t is the number of photons that pass directly into the holes of the collimator, S_c is the number of photons that are scattered in the collimator, P_e is the number of photons that penetrate through the collimator, $\mathcal{A}_{tot}$ is the total surface of the collimator, and $\mathcal{A}_{dc}$ is the collimator opening area.

$$SNR = \frac{S_t}{S_c + P_e} * \frac{\mathcal{A}_{tot} - \mathcal{A}_{dc}}{\mathcal{A}_{dc}} \quad \text{(III-2)}$$

By means of error propagation, the uncertainty associated with the SNR is calculated using equation (III-3). Uncertainties associated with the three count values are estimated making the assumption of a Poisson behavior. It is assumed that the area calculations are accurate. The terms in equation (III-3) are identical to those in equation (III-2).

$$\Delta SNR = \frac{\mathcal{A}_{tot} - \mathcal{A}_{dc}}{\mathcal{A}_{dc}} * \frac{1}{(S_c + P_e)} * \sqrt{S_t + \frac{S_t^2}{S_c + P_e}} \quad \text{(III-3)}$$

3) Results

In this part, MC simulation results (paragraph II.C) of the SNR for the different collimator configurations studied (paragraph 1), are presented. In order to take into account the trade-off between manufacturing cost and collimator performances, it was chosen to express SNR values as a function of the number of holes required to manufacture the studied collimator. The traditional manufacture of a tungsten collimator can only be achieved by superimposing slices with a maximum thickness of 900 µm.

SNR for each collimator configurations (paragraph 1) are presented in figure 4. The latter shows the evolution of the SNR with the number of holes for each collimator configuration studied.

Results demonstrate that the best collimator configuration in terms of SNR, is the configuration for which the holes diameter is 0.75 mm and the size of septa is 1 mm. They also show that in terms of SNR, it is better to consider a septa size of 1 mm rather than 0.5 mm. In addition, collimators with 1 mm septa offer the best evolution with increasing the collimator thickness.

Finally, the main features of the collimator design was determined with the following configuration: holes with a diameter of 1 mm, septa with dimensions of 1 mm, and a thickness of 6.3 cm. The SNR value of the chosen configuration is estimated to be 9.97 +/- 0.92, it is highlighted by the red arrow in figure 4. This configuration was chosen because it offers the best trade-off in terms of SNR value and manufacturing cost.

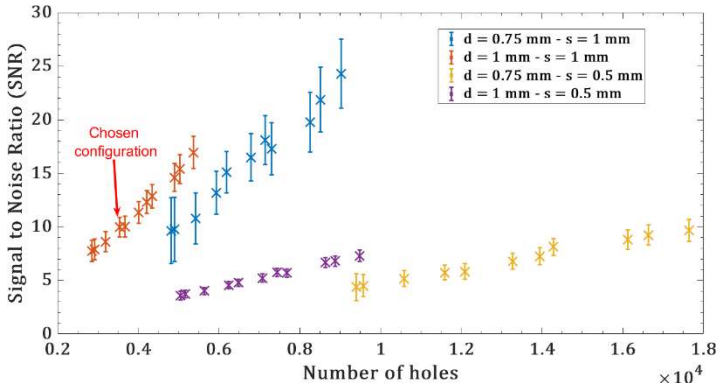

Figure 4: Evolution of the SNR with the number of collimator holes (for a surface of the detector of 2 cm²) for four different configurations of holes/septa: "d" represents the diameter of the holes, "s" is the size of septa. For a given collimator configuration (i.e, same color), the leftmost point corresponds to a collimator thickness of 5 cm, and the rightmost point to a collimator thickness of 9.5 cm. Error bars are at 2 sigmas.

IV. Experimental measurements

A. Manufacturing of the system

The final system is composed of two main elements: the WidePIX detector (paragraph II.A) and a collimator designed by MC simulations (paragraph III). The manufactured collimator consists of 53 tungsten sheets of 1.2 mm thickness, each of them drilled with 645 holes. Specific attention was taken to check the alignment of the holes in each tungsten sheet. Figure 5 shows the WidePIX detector, the WidePIX detector associated with the manufactured collimator, and an illustration of the pattern and dimensions of the manufactured collimator.

Figure 5: On the left: the WidePIX detector [4]*; at the center: the WidePIX detector associated with the manufactured collimator; on the right: the pattern and dimensions of septa and holes defining the manufactured collimator.*

B. Experimental setup

For the measurements carried out on the multi-sources irradiatior of the LNHB, the developed imaging system is postioned in front of the beam at a distance of 70 cm, as illustrated in figure 6. The system is positioned so that the beam focuses on the center of the sensitive part of the imager with a normal incidence. The communication between the system and the acquisition computer is done with a 20 m long USB cable. Measurements were performed using radioactive sources of Cs-137 and Co-60 whose dose rates at the system are presented in Table IV. Although the dose rates of the LNHB irradiator are lower than the expected dose rate in the hot cell (roughly 500 $mGy.h^{-1}$), these measurements will allow a preliminary assessment of the capabilities of the proposed system.

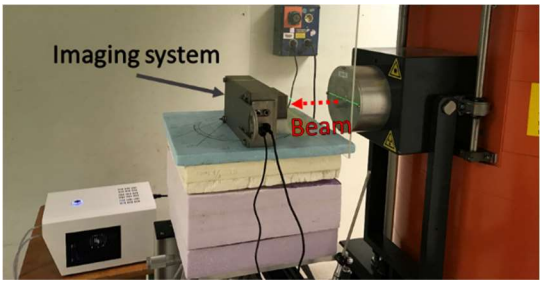

Figure 6: Experimental setup for the measurements on the LNHB multi-sources irradiator.The imaging system is positioned in front of the beam at a distance of 70 cm. On the left side of the picture, the white block is the WidePIX water cooling system.

Table IV: Radionuclides and associated dose rate at the imager used to carry out measurements with the LNHB multi-sources irradiator.

Radionuclide	Dose rate at the system ($mGy.h^{-1}$)
Cs-137	13.59 +/- 0.77
Co-60	33.77 +/- 1.92

C. Raw frame analysis

Measured data with WidePIX correspond to matrix composed of 512×1280 ToT values. When an incoming particule interacts within the CdTe semiconductor, several adjacent pixels may be enlightened, forming a cluster of pixels. In order to estimate the energy deposited by a given incoming particule, it is mandatory to identify each cluster of pixels, such identification is performed using the DBSCAN algorithm [22]. Figure 7 illustrates the use of the DBSCAN algorithm to identify clusters of pixels in a measured frame obtained with the Co-60 source indicated in Table IV.

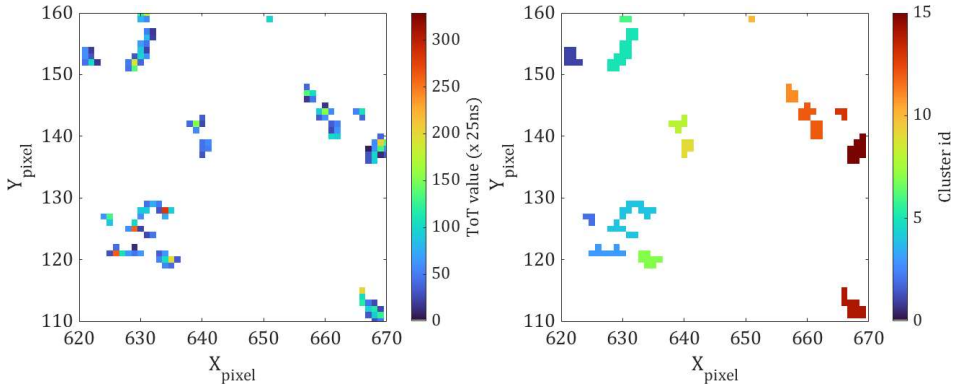

Figure 7: Illustration of clusters identification using DBSCAN algorithm: on the left a measured frame with ToT values deposited on each pixel; on the right, pixels belonging to the same cluster are coloured with the same color.

Once the different clusters of pixels in a given frame have been identified, the ToT spectrum is reconstructed by summing the ToT values in each cluster of pixels. Figure 8 shows measured ToT spectra on the Cs-137 and Co-60 sources described in Table IV. For both measurements, the number of frames is 3600, and the frame duration is 0.01 sec. On the Cs-137 ToT spectrum, the total absorption peak at 661.7 keV is evaluated by means of a gaussian fit, and shows a ToT resolution of 9.1 %. On the Co-60 ToT spectrum, full absorption peaks at 1.173 MeV and 1.332 MeV are not reconstructed, only the Compton edges are distinguishable. For the gamma-rays of Co-60, the main interaction occuring within the semiconductor is Compton scattering, and once scattered, photons may be absorbed. Since the positions of the Compton scattering and the absorption are not the same, the pixel clusters resulting from these interactions will not be geometrically joined. Therefore, they cannot be identified as one interaction, and the total absorption peak is not reconstructed.

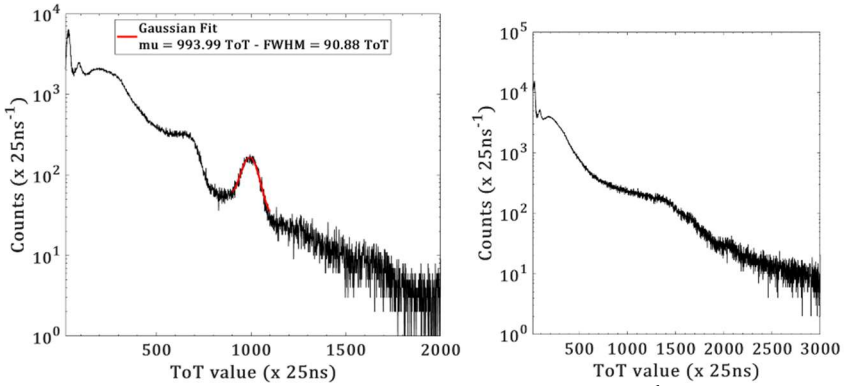

Figure 8: On the left, a measured Cs-137 Time-Over-Threshold spectrum with a 13.59 mGy.h^{-1} dose rate at the system. The fitted (in red) peak corresponds to the full absorption peak at 661.7 keV. On the right, a measured Co-60 Time-Over-Threshold spectrum with a 33.77 mGy.h^{-1} dose rate at the system. For both measurements, the frame duration is 0.01 ms, and the number of frames is 3600.

When reconstructing the measured image, only the interactions whose ToT value corresponds to the total absorption peak at 661.7 keV for the Cs-137 will be considered. This region of interest, correspond to clusters of pixels having a ToT value 993.99 +/- 2×90.88, corresponding to 1.8 % of the total events. About the Co-60, since neither of the two peaks of interest are reconstructed, only interactions depositing a ToT value higher than 1800 will be considered, corresponding to 1.6 % of the total events. ToT values exceeding 1800 correspond closely to the total absorption peaks of Co-60, and as such, any error arising from misidentified events is negligible. Although this selection drastically reduces the counting statistic, it allows all photons that would have scattered in the collimator to be eliminated. On the other hand, in the case of hot cell measurements, the dose rates will be such that this loss in statistics will not be detrimental.

D. Experimental results

1) Collimator geometry characterisation.

The first step in the experimental characterization of the system was to evaluate the geometric parameters of the manufactured collimator. To do this, the whole system is irradiated by the Cs-137 source (Table IV), the positions and dimensions of the different holes are then determined in the measured image. A circular Hough transform based algorithm is used for finding the circles in the measured image [24]. The distributions and theoretical values of the calculated distances between two vertically and horizontally aligned neighbouring hole centers, respectively named $VD_{AjdHoles}$ and $HD_{AligHoles}$, and between two vertically aligned hole centers spaced by one hole, named $VD_{SepaHoles}$, are shown in figure 9. In the latter, values to be compared are $VD_{AjdHoles}$ (2 mm) and μ_1 (2.067 mm), $HD_{AjdHoles}$ and μ_2 (3.46 mm and 3.507 mm), and $VD_{SepaHoles}$ (4 mm) and μ_3 (4.049 mm). The results show that the differences between the experimental results and the expected theoretical values are less than 0.07 mm. For each of the three distributions shown in figure 9, a dispersion of less than 0.06 mm is observed. This value is quite adequate in view of the manufacturing methods of the collimator, and confirms the good mechanical construction of the collimator. This dispersion may be due to the calculation method used, to the intrinsic spatial uncertainty of WidePIX, as well as to potential defects during the manufacturing of the collimator.

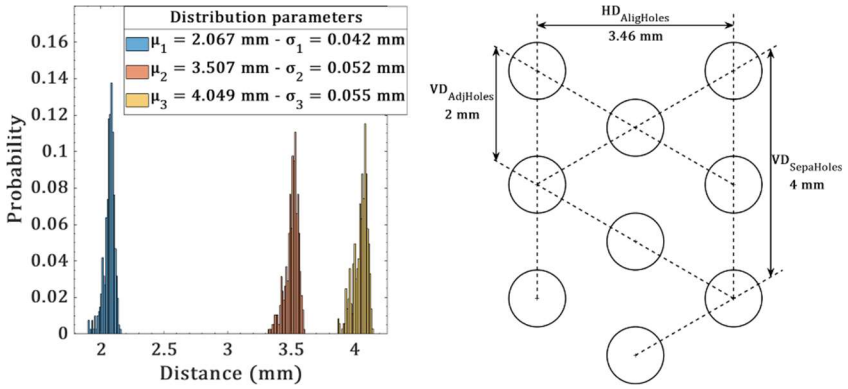

Figure 9: On the left, measured distance distributions (mean values μ, and standard deviations σ) for different collimator elements: in red, the distance between two horizontally aligned hole centers (theoretical value: 2 mm); in blue, the distance between two vertically aligned hole centers (theoretical value: 1.73 × 2 = 3.46 mm); in yellow, the distance between two vertically aligned hole centers spaced by one hole (theoretical value: 4 mm). On the right, a schematic of the different theoritical values: $VD_{AjdHoles}$ and $VD_{SepaHoles}$ correspond, respectively, to the distance between the centers of two vertically aligned holes adjacent to each other (2 mm) and separated by one hole (4 mm); $HD_{AligHoles}$ corresponds to the distance between the centers of two horizontally aligned holes (3.46 mm).

2) Evolution of the number of measured interactions and total ToT deposition according to the frame duration

When making measurements with a pixelated detector based on Timepix technology, a key parameter is the frame duration. The longer the frame duration, the greater the number of interactions measured, but if the frame duration is too long then it is no longer possible to differentiate the pixel clusters generated by the incident particles as they end up overlapping, making them indistinguishable. Figure 10 shows the evolution of the number of measured interactions per frame versus the frame duration for measurements carried out on a Cs-137 source with a dose rate at the system of 13.59 $mGy.h^{-1}$, and two examples of measured frame of 0.01 sec and 0.1 sec. Results show a linearity between the number of measured interactions per frame with the frame duration up to 0.01 sec. For a frame duration greater than 0.1 sec the number of measured interactions is undersestimated. This is due to an overlap of the interactions in the clusters of pixels, this effect is illustrated on the two frames shown in figure 10. This highlights the importance of choosing a frame duration adapted to the irradiating object being measured, especially since the WidePIX detector has a dead time of 0.2 sec per frame.

However, although in the case of a frame duration not adapted to the activity of the source to be imaged, the number of interactions identified is underestimated; the value of energy deposited per frame (measured by means of the ToT value) remains linear with the frame duration, as illustrated in figure 11. This figure shows the evolution of the total ToT deposition per frame with the frame duration, for a measurement carried out with the Cs-137 source. Since the ToT values are proportional to the energy deposited by an incoming particle, these results show that the integrated dose per frame in the system can be estimated from the measured ToT values by a linear law, as shown with another Timepix based system in [25].

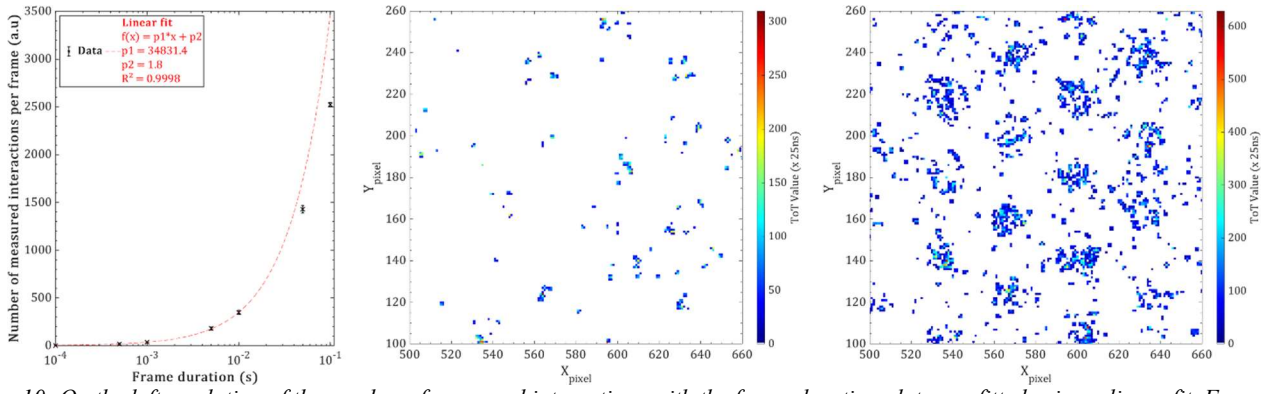

Figure 10: On the left, evolution of the number of measured interactions with the frame duration, data are fitted using a linear fit. For each measurement, the number of frames is 3600. In the center and on the right, respectively, illustrations of a measured frame of 0.01 sec and 0.1 sec. The measurements are carried out with a Cs-137 source inducing a dose rate of 13.59 $mGy.h^{-1}$ at the level of the system.

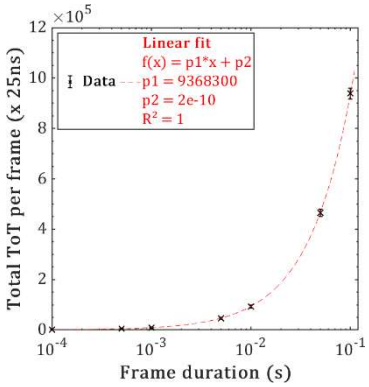

Figure 11: Evolution of the total ToT deposition per frame with the frame duration, data are fitted using a linear fit. For each measurement, the number of frames is 3600. The measurements are carried out with a Cs-137 source inducing a dose rate of 13.59 mGy.h^{-1}at the level of the system.

3) Experimental simulation of swelling.

The main purpose of these developments is to measure and visualize the swelling of a fuel rod following a LOCA sequence. As first estimation of this *phenomena*, two measurements were carried out on the multi-sources irradiator of the LNHB using lead bricks, in order to reproduce a similar configuration in laboratory conditions. Two lead bricks were positioned between the irradiator and the imager, so that the space between the two bricks was initially 5.5 +/- 0.5 mm and subsequently 9 +/- 0.5 mm. The objective of these measurements was to verify the ability of the system to visualize the distance variation between the two bricks and also to quantify it. A difference of 3.5 mm between the two measurements with the lead bricks was chosen as it corresponds roughly to the expected diameter variation of the fuel rod before and after swelling. An example of images obtained from those measurements is shown in figure 12, the two images represent the number of interactions measured over a summation of 3600 frames of 0.01 sec with a Cs-137 for both distances previously mentioned. The graph in figure 12 corresponds to the summation over the Y_{pixel} of the number of interactions versus $X_{position}$ in the detector in mm, the black line corresponds to a distance of 5.5 mm between the lead bricks, and the red doted line to a distance of 9 mm. One can notice, both on the images and on the graph presented in figure 12, the presence of "spurious" counts on the left side of the images, corresponding to the leftmost peaks (with maximal values lower than 150) on the graph. The assumption explaining the presence of these spurious counts is the possibility that for these measurements the system was slightly tilted with respect to the incident beam. The presence of spurious peaks, induced by potential tilting of the system with respect to the incoming beam, contributes to errors in the approximation of the distance between the lead bricks. Since these errors are not evaluated here, they may be considered a lower limit for this approximation. Future studies will be performed to estimate the tilt of the system, as well as its contribution to the total error in the measurement of the distance between the lead bricks and future measurement with the fuel rod.

Thanks to the graph in figure 12, the distance between the two lead bricks is calculated as the absolute difference in the $X_{position}$ of the two rightmost and leftmost peaks in the signal, not considering the two spurious peaks. The uncertainty as well as the value of the $X_{position}$ of a given peak is estimated by means of a Gaussian fit on the peak considered. The $X_{position}$ corresponds to the mean of the fit, and the uncertainty to twice the standard deviation of the fit. Then, the uncertainty of the calculated distance is estimated by means of error propagation. The calculated distances between lead bricks are 5.50 +/- 0.60 mm (black curve), and 9.13 +/- 0.56 mm (red dotted line).

Figure 13 presents results obtained with this experimental setup, for the Cs-137 and Co-60 sources presented in Table IV, for frame durations ranging from 5×10^{-4} sec up to 0.1 sec. The results show that for all the measurements carried out in this experimental setup, the maximum difference between the calculated distance and the "real" distance between the two lead bricks is not greater than 0.28 mm. The estimated distance between the two lead bricks obtained experimentally does not compensate for the duration of the frames, nor for the type of source used. This can be explained by the experimental set-up (the number of frames, and the dose rates) which ensure sufficient counting statistics.

The results validate the possibility of visualising and quantifying a variation of the order of 3.5 mm on a beam of incident particles. A further study should be carried out to evaluate and quantify the minimum measurement time ensuring a relevant estimation of the distance between the lead bricks.

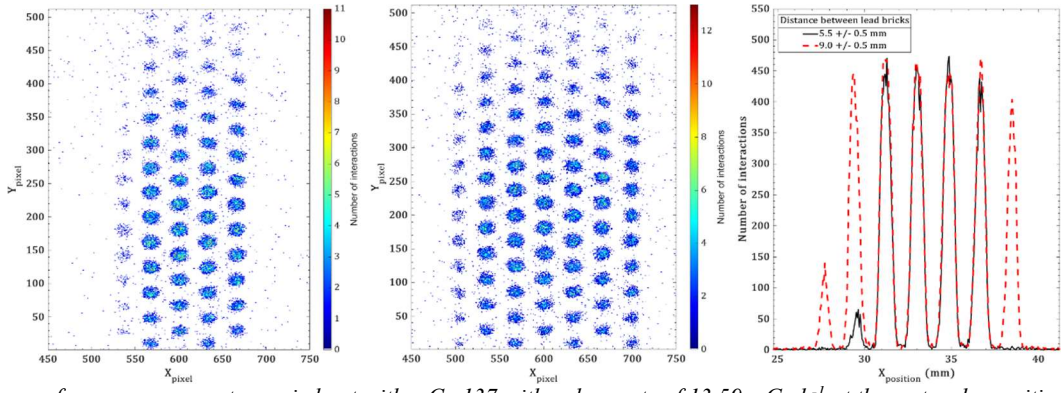

Figure 12: Images from measurements carried out with a Cs-137 with a dose rate of 13.59 mGy.h^{-1} at the system by positionning two lead bricks between the system and the irradiator. Lead bricks are spaced 5.5 mm apart on the left, and 9 mm apart on the right. Both images are obtained from 3600 frames of individual 0.01 sec duration. On the right, projection of the summation over Y_{pixel} of the number of interactions versus $X_{position}$ in the detector in mm, the black line corresponds to a distance of 5.5 mm between the lead bricks, and the red doted line to a distance of 9 mm.

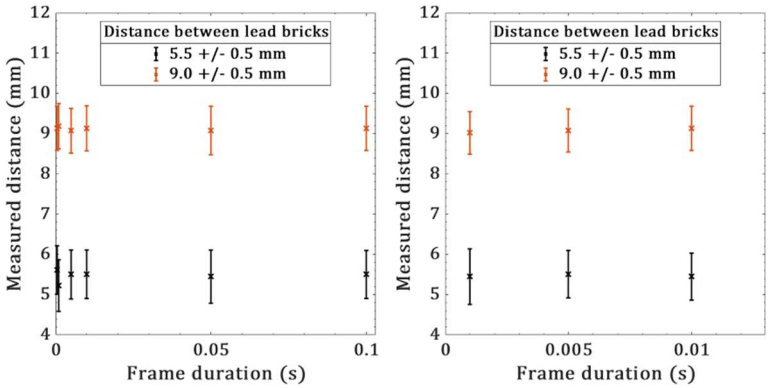

Figure 13: Measured distances between lead bricks (5.5 mm and 9 mm) with the developped system for different frame durations, for each measurements, the number of frame is 3600. Error bars are at 2 sigmas. On the left, measurements are carried out using the Cs-137 source. On the right, measurements are carried out using the Co-60.

V. Conclusion and Future Developments

The objective of this work was to develop a gamma imager prototype able to visualize a 4 to 6 mm variation in the diameter of a fuel rod. The prototype, in addition to having sufficient angular resolution, must be capable of sustaining dose rates of several hundreds of milligrays per hour, and be remotely operated in a hot cell. The developped gamma imager prototype is mainly made of a WidePIX detector and a homemade tungsten collimator. The latter was designed using MC simulations, and consists in a honeycomb pattern. It is made of holes with a diameter of 1 mm, a size of septa of 1 mm, has a thickness of 6.3 cm, and covers the 20 cm² surface of the WidePIX detector.

After this Monte Carlo design step, the system was manufactured and tested with the LNHB Cs-137 and Co-60 multi-sources irradiator. Measurements show the ability of the system to visualize an incoming beam of gamma-rays with a size of 5.5 mm, and evaluate a variation in its dimension of 3.5 mm. These performances are very encouraging for the final tests in the LOCA experiments, in which it is expected to image in real time the 4 mm variation in diameter of a fuel rod.

Developments carried out in the frame of this work open up several prospects for the further developments related to this gamma imager. First, an energy calibration of the system needs to be carried out, this would allow a better energy resolution on the total absorption peak at 661.7 keV [26], which could ultimately translate into a gain in angular resolution, by improving the selection of photons that have not interacted in the collimator. Another perspective concerns the reconstruction algorithm used to visualize the results in order to improve the current one. An extensive study must be conducted to develop an iterative algorithm, based on a MAP-EM (Maximum A Priori-Expectation Maximization) approach, that would take into account the response of the detector, and would introduce an *a priori* on the position and dimensions of the fuel rod to be imaged, increasing the performance of the system.

VI. Acknowledgement

This work would not have been possible without the support and the help of the technicians, engineers and researchers from the LAMIR laboratory of CEA Cadarache. We thank Isabelle Moysan-Lavoine, head of the LAMIR, for allowing us access and hosting us in their facilities. We are especially grateful to Sébastien Bernard, Bruno Biard, Lawrence Halladjian and Kélian Ronne for their help and advices during the developments.

VII. References

[1] B. Biard *et al.*, "The VINON-LOCA test facility : exploring the LOCA phenomenology through an out-of-pile thermal sequence on irradiated pressurized fuel rod," vol. 06002, pp. 1–5, 2021, doi: https://doi.org/10.1051/epjconf/202125306002.

[2] "EDF, Electricité de France." [Online]. Available: https://www.edf.fr/.

[3] "Framatome." [Online]. Available: http://www.framatome.com/FR/accueil-57/index.html.

[4] "Widepix." [Online]. Available: https://advacam.com/camera/widepix-21x5-mpx3.

[5] R. Ballabriga, M. Campbell, E. Heijne, X. Llopart, L. Tlustos, and W. Wong, "Nuclear Instruments and Methods in Physics Research A Medipix3 : A 64 k pixel detector readout chip working in single photon counting mode with improved spectrometric performance," *Nucl. Inst. Methods Phys. Res. A*, vol. 633, pp. S15–S18, 2011, doi: 10.1016/j.nima.2010.06.108.

[6] J. Jakubek, "Nuclear Instruments and Methods in Physics Research A Precise energy calibration of pixel detector working in time-over-threshold mode," *Nucl. Inst. Methods Phys. Res. A*, vol. 633, pp. S262–S266, 2011, doi: 10.1016/j.nima.2010.06.183.

[7] M. J. Cieślak, K. A. A. Gamage, and R. Glover, "Coded-aperture imaging systems: Past, present and future development – A review," *Radiat. Meas.*, vol. 92, pp. 59–71, 2016, doi: 10.1016/j.radmeas.2016.08.002.

[8] S. R. Gottesman and E. E. Fenimore, "New family of binary arrays for coded aperture imaging," *Appl. Opt.*, vol. 28, no. 20, p. 4344, 1989, doi: 10.1364/ao.28.004344.

[9] S. Sun, Y. Liu, and X. Ouyang, "Near-field high-resolution coded aperture gamma-ray imaging with separable masks," *Nucl. Instruments Methods Phys. Res. Sect. A Accel. Spectrometers, Detect. Assoc. Equip.*, vol. 951, p. 163001, 2020, doi: https://doi.org/10.1016/j.nima.2019.163001.

[10] R. Accorsi and R. C. Lanza, "Near-field artifact reduction in planar coded aperture imaging," *Appl. Opt.*, vol. 40, no. 26, pp. 4697–4705, Sep. 2001, doi: 10.1364/AO.40.004697.

[11] K. Van Audenhaege, R. Van Holen, S. Vandenberghe, C. Vanhove, S. D. Metzler, and S. C. Moore, "Review of SPECT collimator selection, optimization, and fabrication for clinical and preclinical imaging," *Med. Phys.*, vol. 42, no. 8, pp. 4796–4813, Aug. 2015, doi: 10.1118/1.4927061.

[12] D. L. Bailey, I. A. E. Agency, J. Humm, A. Todd-Pokropek, and A. van Aswegen, *Nuclear Medicine Physics: A Handbook for Teachers and Students*. International Atomic Energy Agency, 2015.

[13] J. T. Goorley *et al.*, "Initial MCNP6 Release Overview - MCNP6 version 1.0," 2013.

[14] L. Patarin, *Le cycle du combustible nucléaire*. 2002.

[15] "Laraweb," 2016. [Online]. Available: http://www.nucleide.org/Laraweb/index.php.

[16] "Laboratoire National de Métrologie et d'Essais (LNE)." [Online]. Available: https://www.lne.fr/en.

[17] "COFRAC accreditation." [Online]. Available: https://www.cofrac.fr/en/.

[18] "LNHB, Cobalt and ceasium irradiators." [Online]. Available: http://www.lnhb.fr/presentation-en/cobalt-and-cesium-irradiators/.

[19] "Nuclear Fields." [Online]. Available: https://www.nuclearfields.com/index.htm.

[20] B. Camanzi, "Imaging and detectors for medical physics, Lecture 5: Gamma cameras," *Joint CI-JAI advanced accelerator lecture series, University of Oxford*, 2016.

[21] M. Berger and J. Hubbel, "XCOM Photon Cross Sections," *Iaea.Org*, 1987.

[22] M. Ester, H. Kriegel, J. Sander, and X. Xu, "A density-based algorithm for discovering clusters in large spatial databases with noise," in *2nd International Conference on Knowledge Discovery and Data Mining*, 1996, doi: 10.1.1.71.1980.

[23] G. Amoyal, Y. Menesguen, V. Schoepff, F. Carrel, N. Blanc de Lanaute, and J. C. Angélique, "Evaluation of Timepix3 Si and CdTe hybrid pixel detectors spectrometric performances on X- and gamma-rays," *IEEE Trans. Nucl. Sci.*, vol. 68, pp. 229–235, 2021, doi: 10.1109/TNS.2020.3041831.

[24] J. Illingworth and J. Kittler, "The Adaptive Hough Transform," *IEEE Trans. Pattern Anal. Mach. Intell.*, vol. PAMI-9, no. 5, pp. 690–698, 1987, doi: 10.1109/TPAMI.1987.4767964.

[25] G. Amoyal, V. Schoepff, F. Carrel, V. Lourenco, D. Lacour, and T. Branger, "Metrological characterization of the GAMPIX gamma camera," *Nucl. Instruments Methods Phys. Res. Sect. A Accel. Spectrometers, Detect. Assoc. Equip.*, vol. 944, p. 162568, 2019, doi: 10.1016/j.nima.2019.162568.

[26] J. Jakubek, "Precise energy calibration of pixel detector working in time-over-threshold mode," *Nucl. Instruments Methods Phys. Res. Sect. A Accel. Spectrometers, Detect. Assoc. Equip.*, vol. 633, no. SUPPL. 1, pp. S262–S266, 2011, doi:

468 10.1016/j.nima.2010.06.183.